

## Zeff profile measurements from bremsstrahlung imaging in the MAST spherical tokamak

A. Patel, P. G. Carolan, N. J. Conway and R. J. Akers

Citation: *Rev. Sci. Instrum.* **75**, 4944 (2004); doi: 10.1063/1.1808915

View online: <http://dx.doi.org/10.1063/1.1808915>

View Table of Contents: <http://rsi.aip.org/resource/1/RSINAK/v75/i11>

Published by the [American Institute of Physics](#).

---

### Related Articles

Soft x-ray spectroscopy of an imploding aluminum liner Z pinch

*Appl. Phys. Lett.* **31**, 477 (1977)

Experimental simulation of a gaseous divertor: Measurements of neutral density inside the plasma

*Phys. Fluids B* **3**, 834 (1991)

Characterization of BCl<sub>3</sub>/N<sub>2</sub> plasmas

*J. Appl. Phys.* **94**, 2199 (2003)

The PBXM Thomson scattering system

*Rev. Sci. Instrum.* **61**, 2906 (1990)

A fiber-optic interferometer for in situ measurements of plasma number density in pulsed-power applications

*Rev. Sci. Instrum.* **74**, 3324 (2003)

---

### Additional information on *Review of Scientific Instruments*

Journal Homepage: [rsi.aip.org](http://rsi.aip.org)

Journal Information: [rsi.aip.org/about/about\\_the\\_journal](http://rsi.aip.org/about/about_the_journal)

Top downloads: [rsi.aip.org/features/most\\_downloaded](http://rsi.aip.org/features/most_downloaded)

Information for Authors: [rsi.aip.org/authors](http://rsi.aip.org/authors)

### ADVERTISEMENT

  
**AIP**Advances

*Submit Now*

**Explore AIP's new  
open-access journal**

- **Article-level metrics  
now available**
- **Join the conversation!  
Rate & comment on articles**

# $Z_{\text{eff}}$ profile measurements from bremsstrahlung imaging in the MAST spherical tokamak

A. Patel, P. G. Carolan, N. J. Conway, and R. J. Akers

EURATOM/UKAEA Fusion Association, Culham Science Centre, Abingdon, Oxfordshire, OX14 3DB, United Kingdom

(Received 10 March 2004; accepted 16 July 2004; published 2 November 2004)

A bremsstrahlung diagnostic has been deployed on the Mega Ampere Spherical Tokamak (MAST), with matrix viewing of the full plasma cross section in a narrow region of the continuum free of spectral lines. An uncooled CCD detector is used to provide 100 Hz  $128 \times 128$  matrix viewing of the plasma emissivity which is spectrally selected using an interference filter of only  $\sim 0.5$  nm bandwidth. The apparently conflicting demands of a large field of view for the plasma and the small solid angle for narrow spectral bandwidth is accommodated in a compact lens, filter, and detector arrangement. Using measured electron temperature and density profiles the  $Z_{\text{eff}}$  profile evolution is determined. [DOI: 10.1063/1.1808915]

## I. INTRODUCTION

The spherical tokamak is a possible concept for a future commercial fusion device. MAST (Ref. 1) is a facility to test the physics of the spherical tokamak in sustained magnetic confined plasmas as well as the wider issues of tokamak physics. Impurity control is important as they play an important role in the plasma performance. For example, H-mode access is aided by vessel boronisation which reduces the oxygen content of the plasma.<sup>1</sup> More generally the presence of impurities in a tokamak plasma affects the particle collisionality, the electrical resistivity and the transport properties as well as diluting the fuel density and reducing the thermal confinement through radiation losses. The impact on collisionality and resistivity of an ensemble of impurity elements and their various ionisation states can be conveniently represented by an effective charge  $Z_{\text{eff}}$  defined by,

$$Z_{\text{eff}} = \frac{\sum_k (n_k Z_k^2)}{\sum_k (n_k Z_k)} = \frac{\sum_k (n_k Z_k^2)}{n_e}, \quad (1)$$

where  $n_e$  is the electron density and  $n_k$  is the density of ions of charge state  $Z_k$ . The related collisional phenomenon of bremsstrahlung is also affected similarly by  $Z_{\text{eff}}$ . Its spectrum,  $S(\omega)$ , is described by

$$S(\omega) \propto \frac{n_e^2 Z_{\text{eff}}^2 \bar{g}_{ff}}{T_e^{1/2}} \exp\left(-\frac{\hbar\omega}{kT_e}\right), \quad (2)$$

where  $\bar{g}_{ff}$  is the Gaunt factor<sup>2</sup> and  $T_e$  is the electron temperature. Thus the need for determining separately the contributions from each ionisation state density to  $Z_{\text{eff}}$  may be circumvented by measuring the bremsstrahlung.<sup>3-6</sup> Operating in the visible to near infrared spectral regions avoids the complicating contribution from the recombination continuum as well as facilitating multiple lines of sight using lenses, fiberoptics, etc. The availability of high performance CCD detector arrays makes the visible particularly advantageous. The detailed measurements now available of the electron temperature and density distributions (e.g., Refs. 7 and 8)

combined with the demands of physics interpretation, particularly in plasma regions with steep thermal gradients (e.g., tokamak transport barriers<sup>9,10</sup>), place greater emphasis on obtaining related measurements with similar temporal and spatial resolution and extent to other profile diagnostics. It was therefore decided that the bremsstrahlung diagnostic should at least fully exploit the MAST Thomson scattering system which provides  $T_e(r)$  and  $n_e(r)$  at 300 points across the plasma diameter at a single time, and at 20 points every 5 ms.<sup>8</sup> In fact, these requirements are exceeded and we can additionally provide off-mid-plane bremsstrahlung measurements, useful in estimating sources of impurity influxes that affect mid-plane and core impurity distributions.

## II. DESIGN

As in most plasma diagnostic systems in magnetic confinement devices there are conflicting requirements. In detecting bremsstrahlung for  $Z_{\text{eff}}$  estimates, high signal to noise ratio (SNR) are increasingly difficult to achieve as the spatial and temporal resolutions are enhanced. Increasing the specifications to accommodate wide plasma viewing and greater spectral purity can also impact on the SNR. Restricted viewing access and the practicality and cost of large optical and detection systems mean that increasing the light throughput to maintain the SNR at the higher specifications has to be considered as a whole in the design optimisation process (e.g., larger detector area versus large spectral filters). The principal factors are the number of chords, the etendue (area times solid angle) of each chord, the bandwidth of the interference filter (to ensure spectral purity), overall field of view (FOV), the detector area and acceptance angle and the acceptable SNR at the desired integration time. Therefore, a holistic approach in optimising the diagnostic element specifications, has been adopted here which encompasses all the components from plasma emission to final detection signal levels.

A schematic diagram of the diagnostic is shown in Fig.

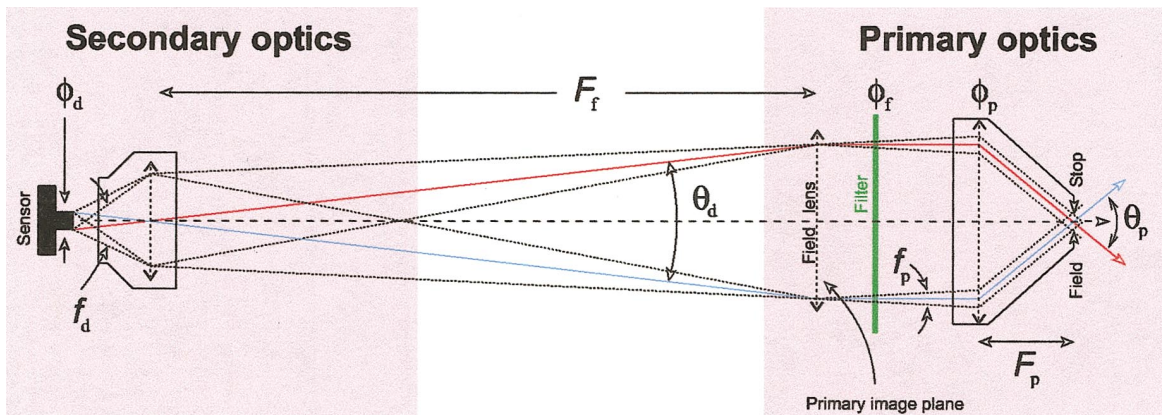


FIG. 1. (Color) Schematic of the imaging diagnostic system. Shown also are chief ray paths of the axis and the edge chords. The circular field stop determines the minimum  $f$ -number incident at the filter.

1. The first component, a field stop, controls the solid angle onto the filter to satisfy the bandwidth requirement on illumination angles but also affecting the throughput. The optical axis of the instrument corresponds to the center of the desired FOV, e.g., the plasma geometrical center. The FOV requirement for MAST is the full horizontal extent of the plasma.

The primary optics section also includes the collection lens, filter, and a field lens. Functionally, it images the plasma telecentrically onto a flat field image plane, the primary image plane where all chief rays are made normal. This is key to the successful use of a single interference filter encompassing a wide FOV. Actually, the filter may be located at any position between the last lens element of the collection lens and the primary image plane.

An interference filter (amplitude division) has high light throughput whilst also preserving full image quality in contrast to grating based systems (wavefront division) with lower throughput, at least at high resolution, and where only linear imaging is possible, at best (for a discussion of throughput gain of the Fabry–Perot compared with a grating spectrometer, see Ref. 11).

Wavelength selection of the system is strictly controlled from application specific filter tolerances and the  $f$ -number of light at the filter. Changing the spectral characteristics of the system is hence simply facilitated by the user defined filter specifications and the field stop diameter.

Coupling of the primary image onto the sensor by the field lens serves one purpose, it converges the filtered light cone to within the aperture of the secondary optics system, reducing the overall length of the diagnostic and the active aperture of the secondary optics.

The design described here is for bremsstrahlung measurement in MAST. However, the design lends itself to other spectral imaging applications in the visible.

The fixed parameters for bremsstrahlung imaging on MAST are: FOV ( $\theta_p$ ), the  $f$ -number at the filter ( $f_p$ ), CCD size ( $\phi_d$ ), and the  $f$ -number subtended by the sensor camera lens ( $f_d$ ) by a high quality, flat field camera lens (Canon  $f$ -1.2L/50 mm). There are also technical constraints such as the sensor specifications (Dalstar 1M30P, www.dalsa.com).

Choice of the field lens focal length ( $F_f$ ) reduces  $\theta_p$  to  $\theta_d$  at the camera lens and determines overall length of the diagnostic.

The above parameters are related as follows. Primary image demagnification,

$$M = f_p/f_d = \theta_p/\theta_d \tag{3}$$

and the required filter diameter is,

$$\phi_f > G(\theta_p)2F_p \tan(\theta_p/2) + \frac{uF_p}{u - F_p f_p} \tag{4}$$

where,  $u$ ,  $F_p$ , and  $G(\theta_p)$  are the object distance, focal length, and the vignetting function of the collection lens, respectively.

Finally, the distance between the field lens and the camera lens is the same as the field lens focal length ( $F_f$ ) for the most compact instrument arrangement. Focal length selection of the (commercial) camera lens,  $F_c$ , is guided by,

$$F_c = F_f/(M + 1). \tag{5}$$

The bremsstrahlung imaging system is compact ( $\sim 0.5$  m) with the following component values:  $\phi_f=50$  mm,  $F_p=68$  mm,  $\phi_p=80$  mm,  $f_p=10$ , FOV (or  $\theta_p$ )= $48^\circ$ , and  $F_f=250$  mm. All components are commercially available with the exception of the custom collection lens which is covered in Sec. III C.

### III. BREMSSTRAHLUNG IMAGING

The MAST vacuum vessel geometry and the tight aspect ratio nature of the ST facilitates full access, allowing the whole plasma cross section to be viewed with no obstructions. A schematic diagram of an equator cross section and the instrument FOV is shown in Fig. 2. The identification of a line free region in the visible is now discussed. The line free bandwidth of the spectrum determines the filter specifications, in particular the centre wavelength and the fastest allowable  $f$ -number.

#### A. Plasma assessment in the visible

Spectral surveys of the visible have been undertaken in conventional tokamaks (e.g., Refs. 4 and 12–14) in search of

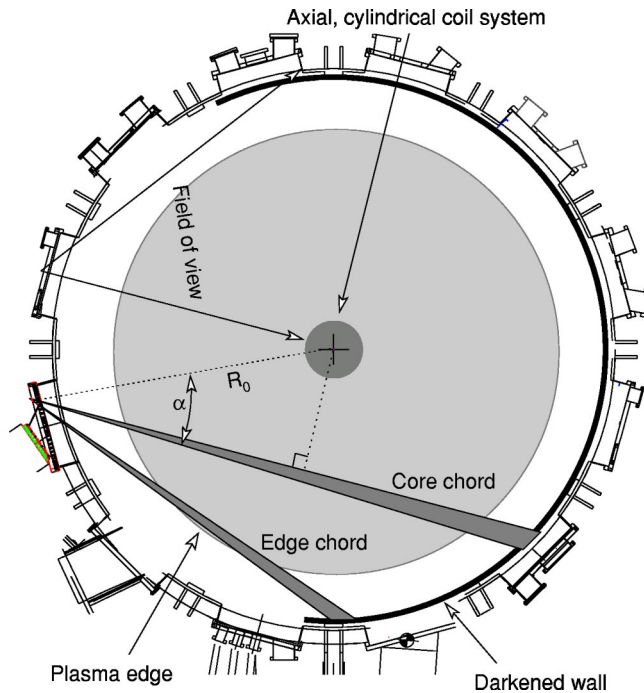


FIG. 2. Schematic equatorial plan view of the MAST vacuum vessel. Large parts of the circumference and the vertical plane of the vessel interior are darkened with colloidal graphite to reduce visible reflections. The bremsstrahlung imaging diagnostic is mounted in one of the large mid-plane ports. The FOV is shown in red. Core and edge view chords (green and blue respectively) from the MAST charge exchange spectroscopy hardware are used here for spectral survey purposes.

line free regions in the visible. Once identified, the measured bremsstrahlung emissivity is used with density and temperature to estimate plasma  $Z_{\text{eff}}$ .<sup>3,5,6</sup>

The bremsstrahlung continuum, however, may be blended with line emission for a given view chord and can lead to unacceptable errors. The importance of line blends is perhaps best appreciated as a function of chord angle  $\alpha$  (see Fig. 2). To show this we have used the MAST charge exchange spectroscopy hardware (see Ref. 15). The diagnostic has several discrete equator chords at different  $\alpha$ . Two such views are shown in Fig. 2, they correspond to the plasma core and edge. Light from the two chords is relayed to two slits at the spectrometer input and then dispersed and imaged onto a test filter (a 2 cavity interference filter, center wavelength 523.5 nm, spectral bandpass=1 nm).

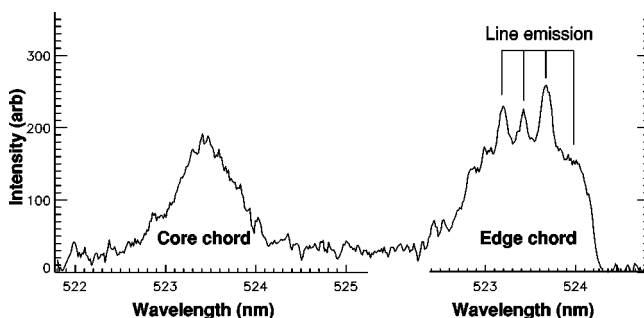


FIG. 3. Spectrally dispersed data corresponding to the edge and core viewing chords. The light is passed through an interference filter for both cases showing a relatively broad filter response with narrower line emission features for the edge chord.

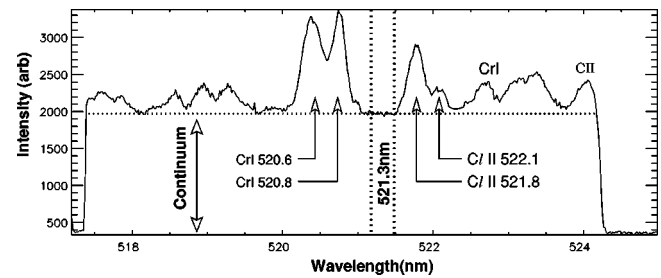


FIG. 4. Spectral survey of the plasma edge at low plasma density. The ratio of line emission to bremsstrahlung is greatest at low densities.

The data for a low density MAST plasma are shown in Fig. 3. Line emission blends with the bremsstrahlung continuum at the plasma edge can be seen. The core chord shows little evidence of line blends. This is consistent with the plasma edge having a higher line to bremsstrahlung brightness ratio since most visible emission is at the plasma edge.

A spectral survey of the MAST plasma edge has identified a narrow wavelength region, free of lines, centered at 521.3 nm (Fig. 4). The line free bandwidth is relatively small, with a spectral bandpass of  $\approx 1$  nm when the survey spectrometer instrument function is taken into account. This allows fastest operation to  $f-9$  for bremsstrahlung imaging (in practise  $f-10$  is used with a 0.5 nm filter). The low density discharge class represents the “worst case scenario” with regard to the contrast between line emission and bremsstrahlung for a chord integrated view because (a) the plasma, in this case, is formed on steel covered poloidal field coils, a likely source of medium- $Z$  visible line emission<sup>16</sup> and (b) the low plasma density means that even weak line emission is detected above the continuum (Fig. 3).

## B. Filter details

Control of the angles of incidence to the filter is important in excluding neighboring line emission. The center wavelength of the filter bandwidth shifts toward the blue when illuminated at an angle  $\theta$  to the normal, given by,

$$\frac{\lambda}{\lambda_0} = \left[ 1 - \frac{1}{n^2} \sin^2 \theta \right]^{\frac{1}{2}} \quad (6)$$

where  $\lambda$  and  $\lambda_0$  are the shifted and unshifted wavelengths and  $n$  is the refractive index. Thus at the extreme of a cone of illumination  $\theta = \tan^{-1}(1/2f_p)$  when the cone axis is normal to the filter. In this way,  $f_p$  controls the maximum angle of deviation from the normal made by the light rays (see Fig. 1). Finite solid angles of illumination are therefore included in specifying the intrinsic bandwidth of the filter to ensure the effective bandwidth is less than the line free extent in the spectrum.

In practise the maximum blue shift of the filter is  $\sim 0.13$  nm as shown Fig. 5 where the full spectral response is shown at the angular cone axis and cone edge ( $\sim 2.8^\circ$ ). For normal operation of the filter the continuum dominates over the line radiation intensity even at the plasma edge. How-

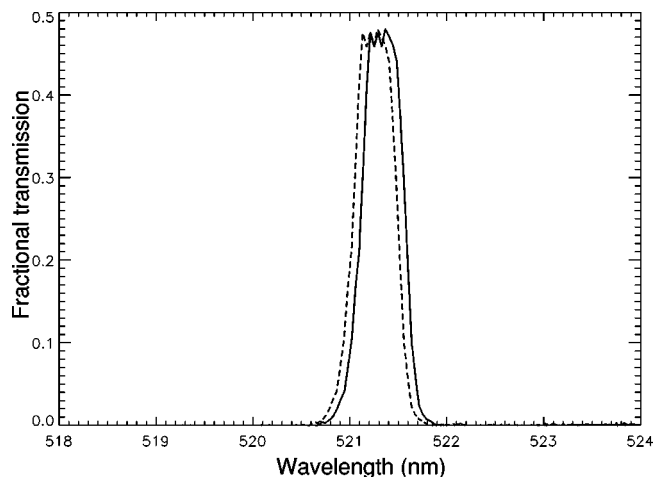


FIG. 5. Filter transmission and the estimated blue shifted transmission (dashed) corresponding to  $f$ -10 illumination at the filter.

ever, line blends, if present, may be unfolded from the raw data of a system with multi chords closely packed such as the one discussed here.

**C. The collection lens**

The component of the primary optics section which gives a combination of the high FOV, acceptable  $f_p$  and a telecentric image is the collection lens. This is an aspheric system, consisting of 3 lens elements in two groups. Two lenses are in an achromatic doublet configuration. A ray trace schematic from the field stop to the primary image plane is shown in Fig. 6 for ray bundles corresponding to three points within the FOV. Vignetting due to the collection optics is known and varies almost linearly with  $\theta_p$ , typically  $<7\%$  at the image periphery. Collection lens parameters are total transmission  $>90\%$ , maximum primary image diameter  $\phi_f \approx 55$  mm and  $f_p \geq 3.4$ .

**IV. RESULTS**

**A. Vessel mapping**

In order to spatially calibrate the pixel row at the equator, the diagnostic framing is synchronised with a photographic quality flash lamp. Vessel features at the equator can be mapped onto pixel numbers and compared with MAST machine specifications.

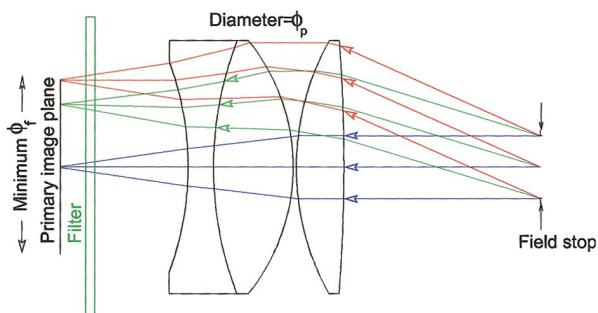


FIG. 6. (Color) Collection lens system, schematic ray trace showing chief rays on axis and one end of the field of view

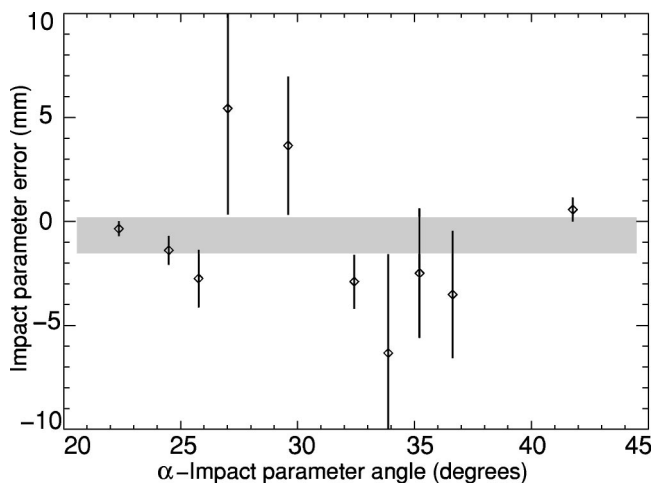


FIG. 7. Mapping results, absolute errors are small,  $|(R_0 \sin \alpha)'| < 0.7$  mm.

Each sensor pixel, or rather the chief ray from it, defines an impact parameter to the vessel axis. Errors between the estimate (from system vignetting) and the mapping between the pixel number and feature edges are shown in Fig. 7 for pixels corresponding to the equator plane. The errors are typically within 1 mm of the impact parameter across the whole FOV. Due to the circularly symmetric nature of the optics, the equator mapping may be extended for all the other planes about the optical axis in order to construct a full two dimensional map of the vessel for chief rays corresponding to all pixels on the sensor.

**B. Diagnostic performance**

The signal to noise ratio is mainly a function of the plasma density [see Eq. (2)], however on-sensor charge-binning allows some control of the signal-to-noise ratio at the expense of the chord count. Table I summarizes some of the chord count configurations used with corresponding signal levels.

**C.  $Z_{\text{eff}}$  and discussion**

Absolute calibration for the full FOV to at least  $\sim 3\%$  error is achievable using a calibrated large-area integrating sphere. The radial bremsstrahlung emissivity is obtained from the chord integrated measurements using the Abel inversion technique.<sup>17</sup> The errors are estimated in the following

TABLE I. Signal levels and chord count of the system for low and higher plasma density operating regimes. The frame rate is 100 Hz (with 7.8 ms integration time), synchronized with other plasma diagnostics but can potentially be as high as 460 Hz with the penalty of reduced signal-to-noise ratio. The principal noise source is shot noise. Likely Abel inversion errors at the geometric axis are from Monte Carlo calculations with added Gaussian noise.

Plasma areal density ( $\times 10^{19} \text{ m}^{-2}$ )	Effective image resolution (pixels)	SNR ratio	Inversion error $\pm \sigma$
$\sim 2$	$128 \times 128$	$> 50$	$< 7.7\%$
$\sim 2$	$256 \times 128$	$> 30$	$< 11.4\%$
$> 3$	$128 \times 128$	$> 150$	$< 3\%$
$> 3$	$256 \times 128$	$> 100$	$< 4.1\%$

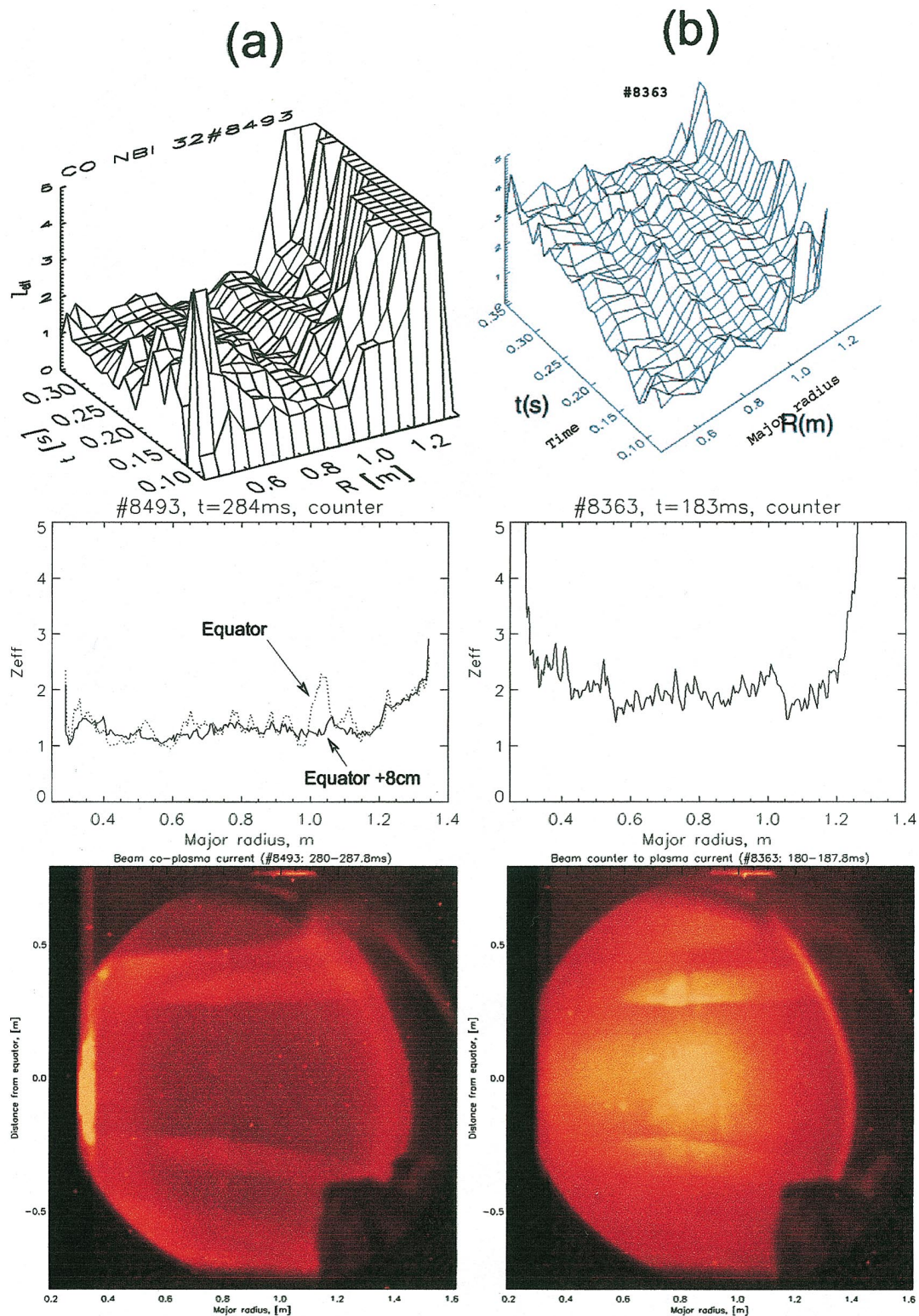


FIG. 8. (Color) Plasma- $Z_{\text{eff}}$  profile evolutions for a neutral beam that is (a) co- and (b) counter-to the plasma current. High resolution, single time point  $Z_{\text{eff}}$  profiles are also shown. The “counter” discharge shows a flat, but increasing,  $Z_{\text{eff}}$  profiles. For most MAST discharges the  $Z_{\text{eff}}$  values are generally in the region 1–1.5.

way: projections of an emissivity profile, superimposed with Gaussian noise of various magnitudes, are Abel inverted and compared with the original profile. The process is iterated 1000 times to generate Monte Carlo noise statistics for the recovered emissivity profile. As a guide, errors for various signal levels at the plasma axis are shown in Table I. Error

amplification or propagation from the outer shell inward in this technique is adequate at present but a “forward” approach is planned (e.g., Ref. 18).

The velocity averaged Gaunt factor,  $\bar{g}_{ff}$ , for a tokamak plasma, is mainly a weak function of electron temperature but less sensitive to the ion species or ion charge at the

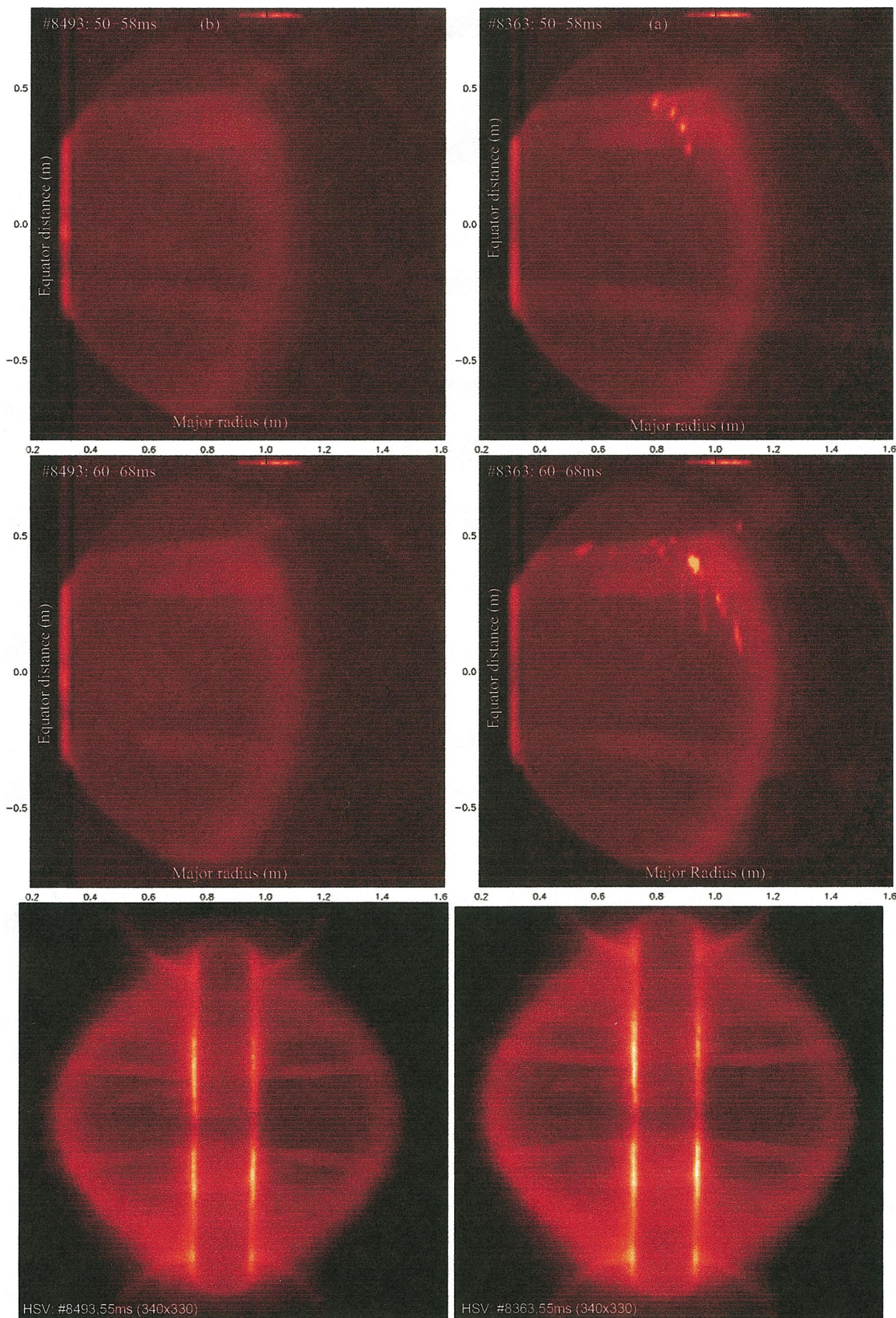


FIG. 9. (Color) Two consecutive bremsstrahlung images for (a) standard (left upper, left center) and (b) “counter” discharges (right upper and center). Emission features near the upper poloidal field coil are seen in the bremsstrahlung case but absent in the unfiltered visible imaging case (lower left and right).

wavelengths of interest here. An empirical form,  $\bar{g}_{ff}=a + b \ln T_e$ , has been used here where  $a$  and  $b$  are constants (for an alternative form, see Ref. 6). The measured equator density and temperature profiles<sup>8</sup> are then used to obtain the bremsstrahlung radial emissivity that correspond to unity plasma- $Z_{\text{eff}}$  at  $\lambda_0$ . Plasma- $Z_{\text{eff}}$  is the ratio of the two radial emissivities.

Results in space and time for a low density ( $n_e \approx 2.8 \times 10^{19}/m^3$ ,  $T_e \approx 2$  keV) neutral particle beam heated discharge (power  $\sim 1.8$  MW) and a “counter” current injected beam heated discharge ( $n_e \approx 5 \times 10^{19}/m^3$ ,  $T_e \approx 0.9$  keV, power  $\sim 1.85$  MW) are shown in Figs. 8(a) and 8(b), respectively.

The emission feature near the plasma edge is located in the separatrix region and is consistent with neutral-disassociation pseudocontinuum radiation observed elsewhere.<sup>19</sup> The standard MAST discharge has  $Z_{\text{eff}}$  close to unity along the equator and for most of the discharge duration [Fig. 8(a)]. The high chord count, 2D and contiguous nature of the diagnostic is demonstrated here: reflection from a single undarkened port plate at the equator is seen in the inverted data, at  $\sim 1.05$  m, but is absent away from the port.

The “counter” current injected discharge [Fig. 8(b)] develops a peaked bremsstrahlung emission core, this is mainly due to density peaking [see Eq. (2)] as the  $Z_{\text{eff}}$  profile is flat. The increase in  $Z_{\text{eff}}$  from  $\sim 1.5$  to  $\sim 3$  is consistent with increased impurity efflux from the plasma poloidal field coils (as indicated in consecutive frames in Fig. 9). Bright features are seen near the top of the plasma in Fig. 9 in the bremsstrahlung imaging system but absent in the unfiltered visible camera (dominated by Balmer  $D_\alpha$  light) and are only observed for some reversed plasma current discharges.

Although we have demonstrated the suitability of compact instrumentation in providing wide field-of-view, 2D imaging for measurement of the bremsstrahlung continuum, the process has obvious extensions to spectral line emission imaging. Optical dissection, by various means allows multiple wavelength imaging providing exact mapping of related physics phenomena. These and related applications are addressed in papers that will be submitted for publication in Review of Scientific Instruments following the High Temperature Plasma Diagnostics conference, 19–22 April 2004, San Diego, CA.

## ACKNOWLEDGMENTS

The authors would like to thank M. J. Walsh for a seminal discussion and C. A. Bunting, K. Hawkins, and M. Price for technical contributions. This work was funded jointly by the United Kingdom Engineering and Physical Sciences Research Council and by EURATOM.

- <sup>1</sup>A. Sykes, J.-W. Ahn, R. Akers, E. Arends, P. G. Carolan, G. F. Counsell, S. J. Fielding, M. Gryaznevich, R. Martin, M. Price, C. Roach, V. Shevchenko *et al.*, *Phys. Plasmas* **8**, 2101 (2001).
- <sup>2</sup>W. Karzas and R. Latter, *Astrophys. J.* **6**, 167 (1961).
- <sup>3</sup>K. Kadota, M. Otsuka, and J. Fujita, *Nucl. Fusion* **20**, 209 (1980).
- <sup>4</sup>P. D. Morgan and J. J. O'Rourke, “Controlled fusion and plasma physics,” 14th European Conference, Madrid, 22–26 June 1987. Contributed papers. Part 3. European Physics Society, 1987, pp. 1240–1243.
- <sup>5</sup>M. E. Foord, E. S. Marmar, and J. L. Terry, *Rev. Sci. Instrum.* **53**, 1407 (1982).
- <sup>6</sup>A. T. Ramsey and S. L. Turner, *Rev. Sci. Instrum.* **58**, 1211 (1987).
- <sup>7</sup>M. N. A. Beurskens, C. J. Barth, N. J. L. Cardozo, and H. J. van der Meiden, *Plasma Phys. Controlled Fusion* **42**, 225 (2000).
- <sup>8</sup>M. J. Walsh, E. R. Arends, P. G. Carolan, M. R. Dunstan, M. J. Forrest, S. K. Nielsen, and R. O’Gorman, *Rev. Sci. Instrum.* **74**, 1663 (2003).
- <sup>9</sup>J. W. Connor and H. R. Wilson, *Plasma Phys. Controlled Fusion* **42**, R1 (2000).
- <sup>10</sup>P. G. Carolan, A. R. Field, H. Meyer, C. D. Challis, G. Cunningham, A. Kirk, M. Valovic, R. Akers, E. Arends, P. J. Catto, N. J. Conway, G. F. Counsell *et al.*, in Proceedings of the 19th International Conference on Fusion Energy 2002, Lyon, France, 14–19 October 2002. IAEA-CN-94/ (EX/C2-6) Conference Proceedings (2002).
- <sup>11</sup>P. Jacquinot, *J. Opt. Soc. Am.* **44**, 761 (1954).
- <sup>12</sup>K. H. Behringer, W. W. Engelhardt, L. Horton, M. F. Stamp, H. P. Summers, M. von Hellerman, M. J. Forrest, and N. J. Peakock, in Proceedings of the 13th International Symposium on Physics of Ionized Gases, Siberian, 1986, p. 281.
- <sup>13</sup>P. D. Morgan, JET contributed papers to the 15th European Conference on Controlled Fusion and Plasma Heating, Dubrovnik, Yugoslavia, 16–20 May 1988. Joint European Torus JET, 1988, pp. 153–156.
- <sup>14</sup>D. G. Whyte *et al.*, *Nucl. Fusion* **38**, 387 (1997).
- <sup>15</sup>P. G. Carolan, N. J. Conway, C. A. Bunting, P. Leahy, R. O’Connell, R. Huxford, C. R. Negus, and P. D. Wilcock, *Rev. Sci. Instrum.* **68**, 1015 (1997).
- <sup>16</sup>I. Lehané, R. Akers, R. Buttery, P. Carolan, M. Gryaznevich, H. Meyer, A. Patel, G. Turri, and S. Cowley, *Europhysics Conference Abstracts* **27A**, P-3.92, EPS, St. Petersburg, Russia, 2003.
- <sup>17</sup>I. H. Hutchinson, *Principles of Plasma Diagnostics* (Cambridge University Press, Cambridge, 1987).
- <sup>18</sup>A. T. Ramsey and M. Dieso, *Rev. Sci. Instrum.* **70**, 380 (1999).
- <sup>19</sup>E. S. Marmar, R. L. Boivin, R. S. Granetz, J. W. Hughes, B. Lipshultz, S. McCool, D. Mossesian, C. S. Pitcher, J. E. Rice, and J. L. Terry, *Rev. Sci. Instrum.* **72**, 940 (2001).